

ARTICLE OPEN



Investigating the mechanical behaviour of Fukushima MCCI using synchrotron X-ray tomography and digital volume correlation

Charilaos Paraskevoulakos¹✉, Joachim Paul Forna-Kreutzer², Keith R. Hallam¹, Christopher P. Jones¹, Thomas B. Scott¹, Clemence Gausse³, Dong Liu⁴, Christina Reinhard⁵, Claire L. Corkhill³ and Mahmoud Mostafavi⁶

A primary target towards the clean-up operation of the Fukushima disaster is the retrieval of Molten Core–Concrete Interaction (MCCI) products, presently residing on the basement of the damaged nuclear reactor Units 1–3. MCCI is a fusion of materials, composed of both nuclear fuel cladding and neighbouring structural components. Determining the currently unknown, physical and mechanical properties of MCCI is essential for successful and timely retrieval. In this paper, we aim to experimentally quantify the mechanical properties of a material fabricated to resemble MCCI. A small-scale representative specimen was mechanically tested using Hertzian indentation stepwise loading. Synchrotron X-ray computed tomography was conducted at several loading stages to reveal the sample microstructure and mechanical degradation. The acquired tomograms were analysed by digital volume correlation to measure full-field displacements and strains developed within the sample volume. Young's modulus and Poisson ratio were determined via this combined methodology.

npj Materials Degradation (2022)6:55; <https://doi.org/10.1038/s41529-022-00264-y>

INTRODUCTION

In 2011, a tsunami engulfed the Fukushima Daiichi Nuclear Power Plant (FDNPP) and resulted in a loss of coolant accident that partially melted the boiling water reactor Units 1–3. Despite injecting high-salinity seawater into the reactor cores for emergency cooling, the reactor temperatures rose to in excess of 2000 °C, melting pellets of UO₂ fuel, zirconium cladding and components, such as steel from the containment vessel and concrete¹. After the temperature in the reactor had stabilised below 100 °C, the mixture solidified to a glass-ceramic, known as Molten Core–Concrete Interaction (MCCI). Even now, almost 400 m³ of water are required daily for cooling the damaged reactor vessels, where MCCI is embedded, from the heat generated by the radioactive decay of ¹³⁷Cs and ⁹⁰Sr inventories². The chemical interaction between cooling water and MCCI leads to dissolution of radionuclides. The contaminated cooling water, which leaks from the damaged reactor core, is collected into neighbouring facilities for reprocessing and remediation. However, hazards related to leaks from the contaminated water tanks still persist, while leakage events of radioactive ¹³⁷Cs to the environment are periodically reported². It is, therefore, critical to fully decommission the plant by extracting the highly radioactive waste and store them safely. It is expected that complete decommissioning of FDNPP will take decades, raising concerns about the environmental hazards associated with the entire clean-up process³.

The extremely high dose environment in the damaged FDNPP reactor vessels requires the design and manufacture of advanced-technology robotic equipment to retrieve the embedded MCCI. Secure and effective decommissioning is directly associated with almost negligible disruption of the material integrity during lift-

out operations. Potential failure to satisfy this target could lead to dispersion of highly radioactive material into the surrounding environment, imposing serious radiological health hazards. Thus, precise evaluation of the physical, chemical and, predominantly, mechanical properties of the material embedded within the reactor cores is vital for successful retrieval. It is of paramount importance to focus on the effects of long-term interaction of MCCI residing within the damaged reactors with seawater and cooling water. Chemical alteration of the initially-formed material can drastically affect its mechanical behaviour. A series of studies, discussing the dissolution mechanisms and the formation of new phases during Chernobyl "lavas" aging^{4–6}, can indicate the Fukushima MCCI composition, hence its degradation behaviour, is also time-dependent.

Due to high radioactivity, it is next to impossible to carry out standard mechanical testing on these materials and extract the properties that are required to design retrieval robotic systems. The levels of complexity rise since the material microstructure is considerably heterogeneous.

The interior of the damaged reactors at FDNPP is currently inaccessible. Even mapping the location where MCCI resides has proven considerably challenging⁷. Limited information about the material formed during the meltdown process has been reported from soil analyses in the vicinity of FDNPP, revealing nanofragments of an intrinsic U-phase⁸. Their presence in the soil was associated with debris fragments released to the environment from the reactors. Data collection and experimentation on material acquired from within the reactor has yet to be performed due to access restrictions. It is believed that MCCI behaviour is highly dependent on the type of the reactor as well as the process and conditions during meltdown. Therefore, extracting

¹Interface Analysis Centre, School of Physics, H. H. Wills Physics Laboratory, University of Bristol, Bristol BS8 1TL, UK. ²Bristol Composites Institute (ACCIS), Department of Aerospace Engineering, University of Bristol, Bristol BS8 1TR, UK. ³Immobilisation Science Laboratory, Department of Materials Science and Engineering, University of Sheffield, Sheffield S13JD, UK. ⁴School of Physics, H. H. Wills Physics Laboratory, University of Bristol, Bristol BS8 1TL, UK. ⁵Diamond Light Source Ltd, Harwell Science and Innovation Campus, Didcot, Oxfordshire OX11 0DE, UK. ⁶Department of Mechanical Engineering, University of Bristol, Bristol BS8 1TR, UK. ✉email: chapa@byg.dtu.dk

information about fuel debris-associated material from other nuclear accidents (Three Mile Island^{9,10}; Chernobyl^{11,12}) could lead to erroneous assumptions. However, knowledge associated with surrogate materials created in the laboratory that closely follow the meltdown process could assist with developing a technology that can measure the behaviour of MCCI correctly.

During meltdown, a variety of materials interact, mainly including UO_2 (fuel pellets), zirconium (cladding), stainless steel (reactor vessel components and its cladding) and concrete (construction material). The solidified mixture is a multi-phase, glass-ceramic material. Simulation studies indicate that it is a solid solution linked with hyper-stoichiometric UO_{2+x} ($x < 0.33$), which can be highly porous². It is interesting to note that dissolution of MCCI, occurring after the end of the solidification process, not only created liquor effluents during the shutdown period but has also potentially altered the properties of the primarily-formed material^{13,14}. This is further complicated by the interaction with corrosive seawater used to cool down the reactor during the post-accident early stages. Experimental work performed on 'lava-like' fuel-containing materials, associated with the Chernobyl nuclear accident, has shown that wetting and drying cycles lead to the formation of numerous U-containing products, including studtite ($\text{UO}_4 \cdot \text{H}_2\text{O}$) and rutherfordine (UO_2CO_3)^{12,15}. Further analysis on real Chernobyl "lavas" samples exhibited a variety of chemical alteration processes, including "gel" formation on the sample surface, corrosion of metallic inclusions (Fe, Ni, Cr) present in the matrix and oxidation of U-bearing phases which lead to the formation of secondary uranyl minerals⁴. Chemical alteration in seawater was significantly more intensive for Chernobyl "lavas" when compared to distilled water, raising concerns about the exposure of Fukushima MCCI to seawater immediately after the meltdown and its effects on the material behaviour⁵. Correlation between the mechanisms of chemical alteration and mechanical degradation plays a key role in understanding such materials behaviour in the long term. Visual inspection on real dry Chernobyl "lava" samples, conducted 20 years after the accident, revealed a proportion of fragmented cores, while the majority of the samples remained intact⁴. The origin of this self-destruction has been associated with volumetric expansion, resulting from the transformation of the relatively unstable tetragonal ZrO_2 phase to monoclinic phase⁶. The scenario of MCCI self-destruction due to chemical alteration during aging, as partially observed with Chernobyl "lava", needs to be considered prior to FDNPP decommissioning.

Since access to real MCCI is yet not feasible, research on the synthesis of simulant material on a laboratory scale has been undertaken to describe the properties of this material. The relevant studies provide details on the accurate replication of the meltdown process and, consequently, the production of a simulant material to be used for characterisation and testing^{16,17}. Similar attempts have been made for Chernobyl fuel debris¹⁵. An et al. performed a melting and solidification experiment, employing an induction heating technique¹⁷. A mixture of UO_2 pellets, ZrO_2 powder, stainless steel, B_4C powder and Zr pellets was melted at temperatures higher than 2000 °C and subsequently quenched to finally produce MCCI-simulant material. The weight ratios used in the mixture were: 60% UO_2 ; 25% Zr and ZrO_2 ; 14% stainless steel; 1% B_4C —in accordance with the melt composition in FDNPP Unit 1^{18,19}. The final product exhibited a dual-layer configuration—a metal-rich layer located above an oxide-rich layer. The oxide-rich layer contained twice as much UO_2 as the metal-rich layer, whilst the metal-rich layer had an abundance of B_4C . If this dual-layer configuration is close to real FDNPP MCCI, it is expected that this heterogeneity of the material structure would have considerable effects on its mechanical properties.

The dual-layer structure of MCCI-simulant was also validated by Song et al.¹⁶. The two layers were easily separated, exhibiting considerably distinct physical and chemical properties, density

and elemental composition. Similar differences were reported for the mechanical properties of the two layers, without referring to any specific quantitative information. Recently, in a parallel study to that presented in this work, Ding et al.²⁰ developed MCCI-simulant material, containing Ce as a surrogate for Pu, contained within the mixed-oxide fuel $[(\text{U,Pu})\text{O}_2]$ present in the reactor of FDNPP Unit 3. A range of U-Zr-O-containing minerals was formed, in addition to crystalline silicate phases including CaSiO_3 , $\text{CaAl}_2(\text{SiO}_4)_2$, SiO_2 -cristobalite and Ce-bearing percleveite ($\text{Ce}_2\text{Si}_2\text{O}_7$). The material was Fe-rich, owing to the incorporation of stainless steel.

The results obtained from an experimental programme implemented to investigate the mechanical properties of this latter MCCI-simulant are presented and discussed in this paper. Hertzian indentation was employed as a favourable technique for mechanical testing on samples with limited volume, an essential prerequisite for radioactive materials. In conjunction, synchrotron X-ray computed tomography (XCT) was performed at distinct loading stages to reveal loading-induced sample microstructural changes. The acquired tomograms were analysed by digital volume correlation (DVC)^{21–24}, enabling the measurement of the sample internal displacement field, from the initial stage of indenter-specimen contact to mechanical failure. Thus, correlation between the material microstructure and the mechanical behaviour was accomplished, as successfully shown by other researchers studying the mechanical performance of various ductile and quasi-brittle materials^{25–30}. Combining the DVC-measured displacement and strain fields with the corresponding external load applied on the sample proved to be an efficient method to accurately estimate the principal material mechanical properties, including Young's modulus and Poisson's ratio.

RESULTS

Mechanical behaviour

The MCCI-simulant sample and the associated load path, as recorded throughout the entire experimental period, are presented in Fig. 1. The sample shape was asymmetrical due to the complexity of preparation methods. A 3D overview of the sample in contact with the Hertzian indenter is shown in Fig. 1a, while representative 2D orthogonal views, illustrating the asymmetric shape of the sample are also given. Figure 1b illustrates the path adopted from early loading stages to failure.

Peaks demonstrate the maximum force imposed on the sample at every loading stage. Force relaxation is observed to have occurred immediately after topping up the load in each cycle. Blue boxes highlight the time periods when XCT scans were acquired. An external force was applied at a maximum of 20 N for the first loading stage, while the mean value recorded during the force relaxation (XCT scanning) period was 14 N (± 0.3 N). The corresponding loads noted during the second loading stage were 70 N and 55 N (± 1.3 N). After the scan related to the second loading stage was completed, the external load was increased to a maximum of 130 N. During the force relaxation period, a mean load value of 112 N (± 5.9 N) was recorded.

A sudden load drop, indicative of sample failure, occurred while topping up the external force for the fourth loading cycle. The load value noted immediately prior to this decay was equal to 160 N. A second load drop followed during the force relaxation. This second load drop is associated with crack propagation occurring under constant load across the sample thickness—probably due to elevated strain zone developing near the crack front. The corresponding XCT scan was acquired after a load plateau was observed. The mean load value recorded during this scan was 68 N (± 1.9 N).

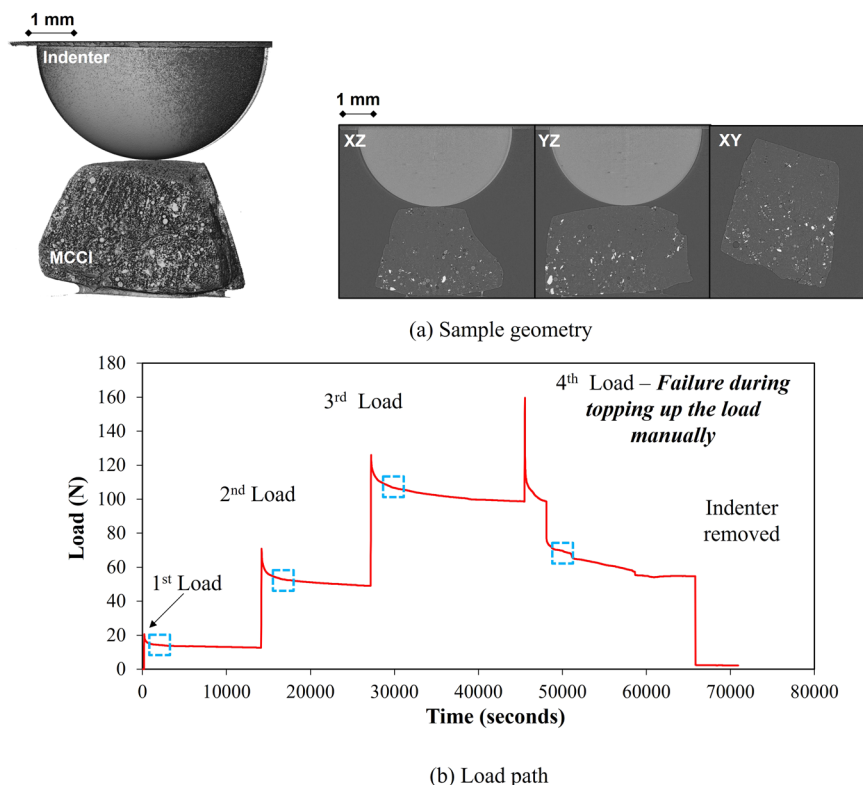


Fig. 1 Representative images. **a** A 3D overview of the MCCI sample (left side) accompanied by a selection of 2D orthogonal views (right side) and **b** the path adopted during loading.

Visualisation and segmentation

A representative cropped 2D image, revealing the strongly heterogeneous microstructure of the MCCI-simulant, is presented in Fig. 2a. The multiphase nature of the sample is evident. The circular features (spherical in 3D) dispersed around the sample surface are typical of iron-rich particles present in the mixture. The bright triangular regions, which correspond to high electron density phases, are attributed to uranium-rich sites. Pores of various sizes are also observed. Differences in the grey-scale intensity range were used to segment the phase volumes, using the relevant modules available in Avizo³¹. The results of this segmentation process are shown in Fig. 2b. The corresponding 3D volumes are shown in Fig. 2c. The original image dataset was cropped to reduce computational time.

In addition to visualisation, quantitative analysis was performed to determine the relevant contained phase volumes. Thus, the iron-rich and uranium-rich phase volume fractions were quantified as was the samples's total porosity. Pores and U-rich phases each occupy <1% of the entire sample volume, while the accumulated spherical Fe-rich phase volume fraction approaches 4%. The $\text{SiO}_2\text{-Al}_2\text{O}_3\text{-CaO}$ matrix is the dominant phase within the investigated sample volume.

The pore size distribution was also determined to investigate the homogeneity of the pores, assuming sphericity equal to one in all occasions. Figure 3 illustrates the corresponding histogram. It is observed that the smaller pores (<50 μm equivalent diameter) dominate within the sample volume. More specifically, 74% of the pores have an equivalent diameter smaller than 20 μm , compared to 25% lying in the 21–50 μm range. Pores with equivalent diameter exceeding 50 μm are only 1.3% of the entire population. In the study of Ding et al.²⁰, who performed high resolution chemical mapping of the same MCCI-simulant, these larger pores were found to accumulate the Pu surrogate, Ce, within their interior, while the smaller ones did not. It is important to note that

these values refer to the entire sample volume. The scan acquired prior to loading was employed for calculations. Computationally-friendly cropped datasets were used to compare between the different loading stages. Thus, the volume of cracks formed after exceeding material strength could be accurately measured.

The evolution of MCCI-simulant mechanical degradation with increasing externally-applied load was investigated, using the 3D tomograms produced after cropping the original dataset. Characteristic views of 3D cuboids generated at all different loading stages are shown in Fig. 4a, probing the same sample volume. The mean load value recorded during the corresponding scan is given beneath each tomographic view. An extended crack network was observed to have formed after the end of the fourth loading cycle, corroborating the assumptions formulated after the sudden drop of force recorded by the load-cell. The crack volume was segmented to probe the entire 3D profile of the sample's mechanical degradation. A characteristic view of the crack volume is given in Fig. 4b, both superimposed with the tomogram and segmented.

Phase volume segmentation was performed on all the datasets produced after the XCT scans were acquired. This process predominantly focused on segmenting only the voids in each tomogram, summing both pore and crack volumes. The voids volume fraction, as calculated for each of the tomograms acquired, is given in Fig. 5.

Volumes were measured using the cropped datasets in all cases. Therefore, a slight difference can be observed between the volume fraction corresponding to the pre-loaded state (zero load) shown in Fig. 5 and the corresponding percentage (<1%) reported previously in the manuscript, where the entire volume dataset was adopted for calculation. The void volume fraction remained almost constant (~2%) as the externally-applied load increased, until the sample failure was observed during the last loading cycle. The data corresponding to the tomogram acquired post-failure (4th load, 68 N) indicated a sharp rise of void volume fraction,

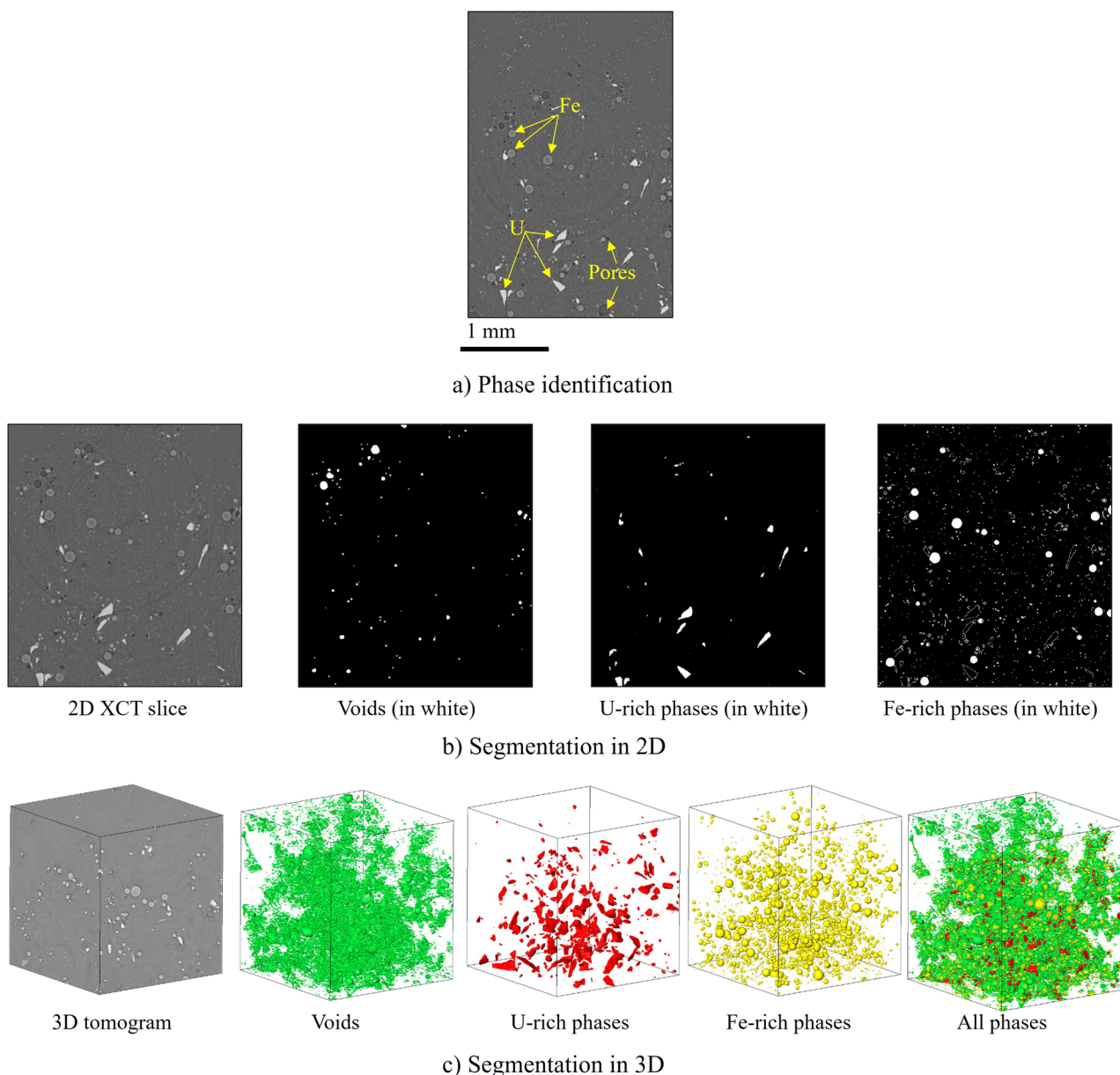


Fig. 2 Representative 2D and 3D images illustrating the multiphase nature of the MCCI simulant. **a** Identification of pores, uranium and iron phases, **b** segmentation of the several phases in a 2D slice, and **c** 3D volumes of the segmented uranium, iron and pore phases.

attributed to the extended crack network formed. A scenario of incremental void volume rise prior to failure would be a sign of potential microcrack formation—a common observation in quasi-brittle material testing.

Digital volume correlation

XCT data were also processed to be used as inputs for DVC analysis. Thus, the full-field displacements and strains developed within the sample volume throughout loading could be determined. The tomogram corresponding to the scan acquired after the initial load (14 N) was applied to the sample, was considered as the reference image dataset. Displacement and strain fields were produced after correlating the reference image dataset with the tomograms associated with higher external loads (55 N; 112 N). The tomogram corresponding to the scan acquired after sample failure (4th load, 68 N) was not included in the DVC analysis since the extended crack network that formed hindered production of reliable displacement and strain maps³².

DVC analysis was conducted using the Avizo ‘XDigital Volume Correlation’ extension module³¹. The original tomograms were processed to minimise computational load. All 32-bit image stacks were converted to 8-bit, using the open-source software ImageJ³¹. Image noise was also reduced by applying despeckle, median and smooth filters³³. Random noise can cause ‘false’ correlation, providing erroneous DVC analysis results. Finally, image stacks were all uniformly cropped to reduce computational load and produce smooth cuboidal volumes. The size of the cropped datasets was 1164 vx × 618 vx × 321 vx (3.77 mm × 2 mm × 1.04 mm).

A twofold method was adopted to determine the displacement and strain fields developed throughout loading. The initial processing step, known as the (subset based) local approach, included the generation of a coarse grid focused on capturing the large displacements occurring within the sample volume. Local DVC computes an average displacement vector at the centre of each sub-set and, therefore, discontinuous displacement maps are initially generated. Interpolation methods are subsequently

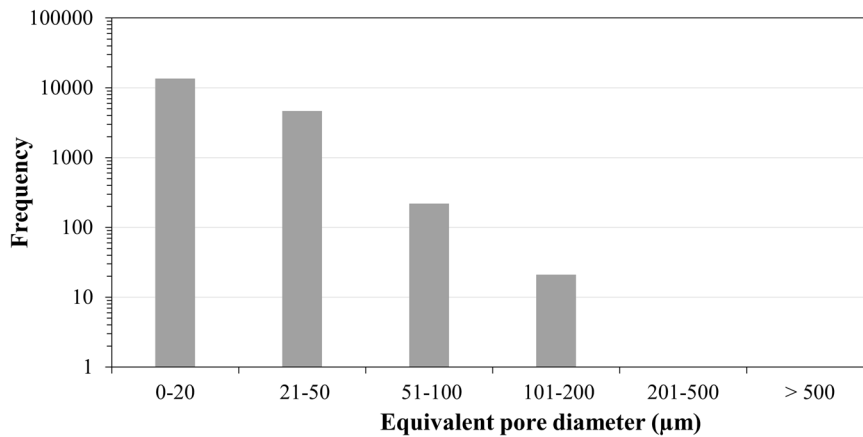


Fig. 3 Pore size distribution for MCCI-simulant mechanically tested on I12 beamline at the Diamond Light Source (DLS).

employed to determine the displacement field at the rest of the grid. The local-DVC displacement field was subsequently fed into a more robust processing algorithm, employed to refine the primarily generated data and produce continuous displacement fields, where the displacement of each node is influenced by neighbouring nodes. This following refined process is known as the finite element (FE)-based global approach. The mesh generated to produce the displacement fields was significantly finer than the grid adopted while employing the local approach.

The above methodology was tested to validate the reliability of the results. Therefore, a virtual displacement field was applied on the reference image dataset. A set of prescribed displacements was imposed on the surface planes of the reference 3D image dataset to generate the deformed dataset for testing. The user-defined axial strains ϵ_{xx} , ϵ_{yy} and ϵ_{zz} were equal to 0.01, 0.011 and 0.02, respectively. DVC analysis was performed, using the reference and deformed image datasets as inputs, to evaluate if the results matched the predefined strain values. A set of input parameters were quantified to correlate the datasets, for both the local and global approaches³¹. The metric and transform ports were set to 'Correlation' and 'Translation + Rotation' modes, respectively. The Correlation threshold was set equal to 0.5. Sensitivity analyses were performed to determine the most suitable sub-volume size for the local approach and mesh size for the global approach. The results are shown in Fig. 6 for various sub-volume sizes. The same process was followed for the global approach. The dotted red lines demonstrate the axial strain values imposed deliberately on the reference image dataset. A good agreement between these values and the corresponding strains determined via the DVC analysis can be observed (Fig. 6b–d), further corroborated by the correlation coefficient²⁵ (Fig. 6a). The ideal mesh sizes, as determined via the sensitivity analysis performed to test the validity of the method, were 0.227 mm (70 pixels) and 0.162 mm (50 pixels) for the local and the global approaches, respectively. Minimum standard deviation for the correlation coefficient values was considered as the key parameter for selecting the optimum mesh size. These numbers were also adopted as inputs to perform DVC analysis on the real datasets.

Two DVC runs were implemented in total. The first was employed to correlate the reference dataset (1st load, 14 N), with the data corresponding to the scan performed after the second loading stage was completed (2nd load, 55 N). The second DVC run was performed to correlate the reference dataset (1st load, 14 N) with the data corresponding to the scan performed after the end of the third loading stage (3rd load, 112 N). Each FE based tetrahedral mesh included 1722 nodes. The correlation coefficient for both DVC runs was 0.925.

The displacement and strain fields developed within the probed sample volume were analysed to investigate MCCI-simulant

mechanical behaviour. In total, three displacement 3D maps were generated to visualise the nodal displacements occurring across all three axes. Accordingly, six strain 3D maps/tensors were implemented, exhibiting both the axial and shear strain distributions. Characteristic views of all the 3D maps generated via DVC analysis are presented in Figs. 7–8. The location of the cropped volumes used to perform DVC analysis is shown in Fig. 7a. The displacements across x, y and z axes are denoted as u_x , u_y and u_z , respectively (Fig. 7b–d). In addition, ϵ_{xx} , ϵ_{yy} and ϵ_{zz} stand for axial strains across the x, y and z axes (Fig. 8a–c), while ϵ_{xy} , ϵ_{xz} and ϵ_{yz} denote the corresponding shear strain distributions (Fig. 8d–f).

The displacement profile across the x axis (u_x) is ostensibly uniform during the transition from the first loading step (14 N) to the second (55 N). However, there is a completely different trend when correlating the data related to the 14 N and 112 N loading cycles. A clear separation between positive and negative displacement values around the middle zone of the cuboid is evident, implying signs of splitting (Fig. 7b). This observation is corroborated by the u_y and u_z displacement maps. Clear concentrations of higher (in absolute values) displacements can be observed around the middle region. Signs of sample splitting are even more distinct if the axial strain maps are considered. The profile of lateral strain ϵ_{xx} (Fig. 8a) reveals a band of higher values around the same area where the shift in u_x displacement was noted.

The ϵ_{xz} map (Fig. 8e) also indicates a localised increase of shear strain in the middle region of the cuboid. It is important to note that the relevant tomograms exhibited no obvious cracks in the locations where DVC data indicated localised elevated axial strains. In addition to visual observation, post-segmentation quantitative analysis revealed no change of the void volume fraction between the first and the third loading stages, as shown in Fig. 5.

Mechanical properties

The DVC-measured data highlighted the qualitative characteristics of the sample mechanical behaviour. Zones of concentrated elevated strains were identified, suggesting locations of potential fracture. In addition to qualitative findings, the full-field displacement and strain data were used to perform a quantitative analysis focused on determining the material mechanical properties. Two alternative approaches, the displacement and strain methods, were adopted to estimate the Young's modulus and Poisson's ratio. Only the DVC-measured displacement data were considered for the displacement method. The mean value of the vertical displacements u_z , corresponding to the top slice of the relative cuboid shown in Fig. 7d, was calculated. Accordingly, the mean vertical displacement of the cuboid bottom slice was determined.

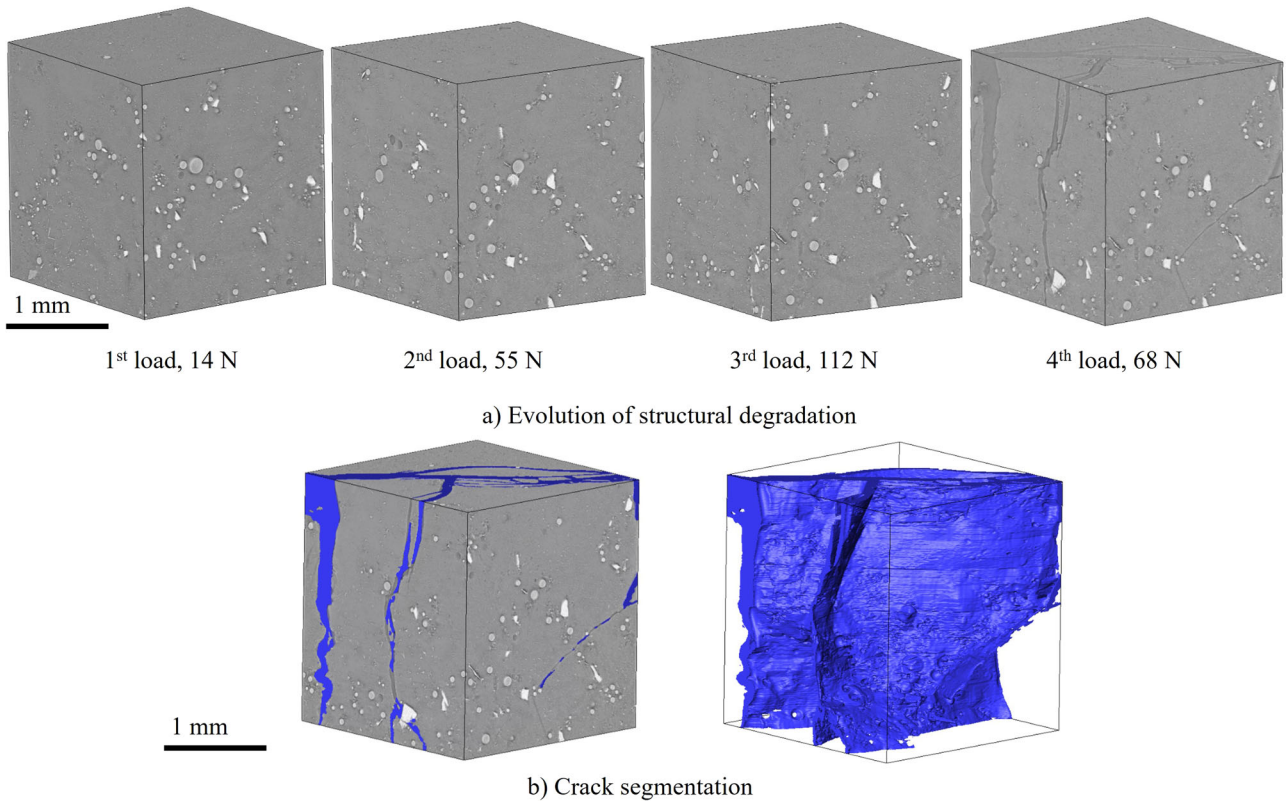


Fig. 4 Characteristic views. **a** 3D tomograms generated after performing XCT scans at several loading stages (from 14 N on the left to post failure 68 N on the right) and **b** segmented 3D crack volume at failure.

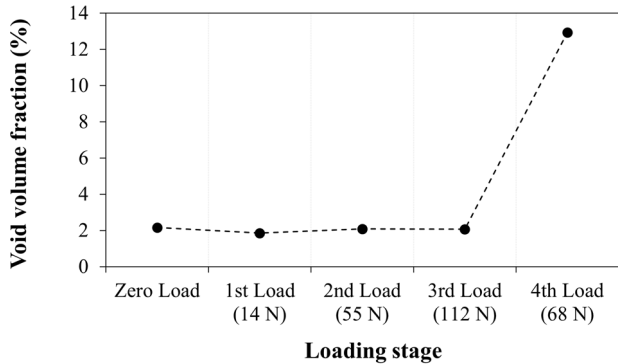


Fig. 5 Evolution of void (i.e. sum of cracks and pores) volume fraction with externally-applied load increase.

The same process was followed to calculate the corresponding mean vertical displacement values for the cuboid shown in Fig. 7d. The absolute difference between the top and bottom mean displacements on each occasion designated the vertical deformation occurred at a specific load-transition phase. The load difference, vertical deformation and geometry of the investigated sample on each occasion were used to determine the relative compressive stress and vertical strain, enabling subsequent calculation of the Young's modulus. Similar concepts have been adopted to reveal the mechanical properties of quasi-brittle, heterogeneous materials based on DVC-measured data²⁹. Separate values for the Young's modulus value were determined for each DVC run. Since two different load transition scenarios were investigated (14 N–55 N; 14 N–112 N), a mean Young's modulus value was calculated.

The strain method was employed to corroborate the results produced via the displacement method. The axial strain values

across the z-axis, denoted as ϵ_{zz} (Fig. 8c), were exported for every element of the FE based mesh. Subsequently, the mean strain value was calculated. In compliance with the displacement method, the load difference on each occasion was divided by the sample surface to calculate the mean compressive stress. Assuming that the material behaviour is elastic in the low loading regime, the Young's modulus was set equal to the ratio between the mean compressive stress and mean compressive strain³⁴. The results produced using both approaches are summarised in Table 1, where E stands for the Young's Modulus. Detailed descriptions of both displacement and strain methods can be found elsewhere³⁴.

Potential stiffness variability within the material volume due to the heterogeneous microstructure was also examined. The DVC analysis exhibited considerably non-uniform axial and shear strain distributions throughout the investigated sample volume, as shown in Fig. 8. Therefore, the variation of the mean vertical strain ϵ_{zz} (Fig. 8c) across the sample height was analysed. All vertical strain values of mesh elements belonging to the same XY plane were averaged. The compressive stress was subsequently divided by this mean XY planar vertical strain to determine the XY planar Young's modulus. The same process was followed for all the different XY planar mean vertical strains calculated across the z-axis. Thus, a potential alteration in material stiffness across the height of the examined DVC volume could be evaluated. The results are given in Fig. 9a. Based on the axis configuration adopted (Figs. 7–8), higher z values reflect locations closer to the sample top surface.

Young's modulus was observed to vary across the sample height. Results revealed a trend of stiffness decay, while moving towards the sample top surface. A similar approach was adopted to estimate the Poisson's ratio of MCCI-simulant. Only the strain fields generated were considered for calculations. Axial strain (ϵ_{xx} ; ϵ_{yy} ; ϵ_{zz}) values were exported for every element belonging to the

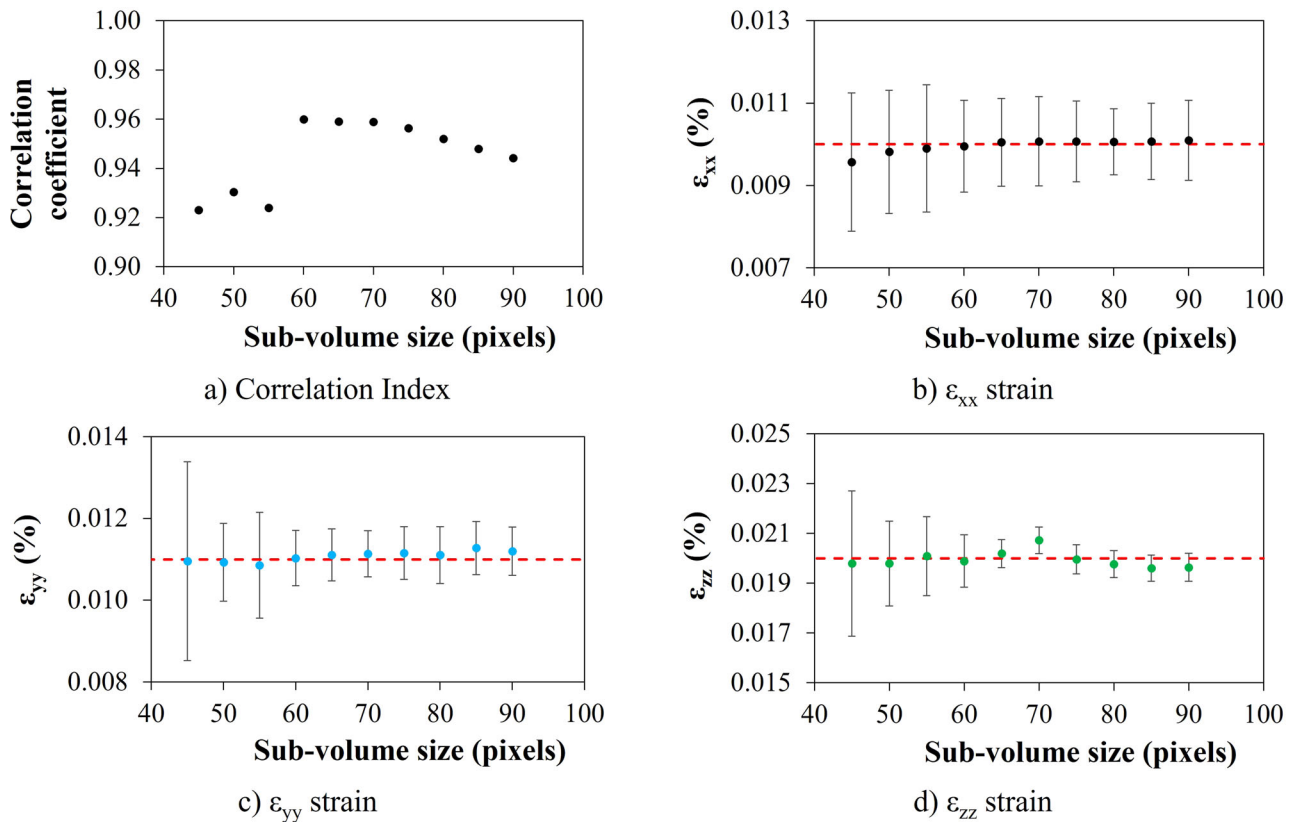


Fig. 6 Sensitivity analysis illustrating the effect of sub-volume size. **a** The correlation index, **b** the axial strains ϵ_{xx} , **c** the axial strains ϵ_{yy} , and **d** the axial strains ϵ_{zz} , after imposing virtual displacements. Error bars, illustrating the standard deviation, are given for each DVC analysis performed.

mesh shown in Fig. 8. Corresponding mean axial strains were subsequently determined. Only the data acquired from the first DVC run (14 N–55 N) were used. The Poisson's ratio ν_{xz} was calculated equal to 0.16 (± 0.3) based on elasticity theory, using Eq. 1.

$$\nu_{xz} = -\frac{\epsilon_{xx}}{\epsilon_{zz}} \quad (1)$$

A large standard deviation error was produced, reflecting the wide scatter of elemental axial strain values. The Poisson's ratio ν_{yz} ($\nu_{yz} = -\epsilon_{yy}/\epsilon_{zz}$) was also calculated to evaluate if the material was isotropic or orthotropic. However, the derived value was outside the range of a continuum (0–0.50) and, therefore, was not considered for further analysis. The Poisson's ratio distribution across the sample height was also investigated, in accordance with the method followed for the Young's modulus. Axial strains ϵ_{xx} and ϵ_{zz} , corresponding to mesh elements lying on the same XY plane (same z coordinate), were averaged. This process was repeated for all the different XY planes composing the DVC volumes. Thus, single mean axial strains were calculated at different sample heights. These mean values were used to derive the corresponding local Poisson's ratios by employing Eq. 1. The change in Poisson's ratio (ν_{xz}) across the height of the DVC-inspected volume is presented in Fig. 9b. Significant variation can be observed.

DISCUSSION

Hertzian indentation loading, combined with XCT performed on a synchrotron beamline and subsequent DVC analysis of the resulting tomograms, proved to be a method for the in-depth investigation of MCCI-simulant microstructure and mechanical performance. Using standard methods of mechanical testing, e.g.

tensile testing, where strain gauges could be adhered to the sample surface and measure the load-induced strain directly, could not be adopted due to the material's radioactive nature. The regulations related to working with ionising radiation-imposed limitations regarding the sample volume, favouring indentation as the only method where a limited sample volume could be investigated under external loading.

Acquired tomograms and successive phase segmentation and quantitative analysis provided information about the heterogeneous material microstructure. The dominant SiO_2 -rich matrix is expected to govern the mechanical performance of the MCCI-simulant. However, the presence of Fe-rich spherical particles, U-rich phases and pores scattered within the microstructure, even at low fraction percentages, would also be expected to affect the mechanical behaviour.

Recorded loading time history, along with visual observation and quantitative analysis of the XCT data, revealed the brittle nature of the sample failure. No signs of typical quasi-brittle behaviour, such as microcrack formation, were identified. This can prove to be a useful finding, assisting the decommissioning process of FDNPP on condition that the behaviour of the surrogate material approaches that of the real MCCI residing in the damaged reactor beds. Brittle failure is associated with complete loss of material integrity after exceeding ultimate strength, a fact that is required to be considered when designing the robotic fleet for decommissioning. However, the acquired data and the analysis performed do not guarantee that the MCCI-simulant; and thus potentially the real Fukushima MCCI, is a brittle material. Although the absence of micro cracks in the XCT data, forming throughout loading, and the constant voids volume until failure imply material brittleness, the DVC data revealed discontinuities, possibly associated with the formation of a microcrack.

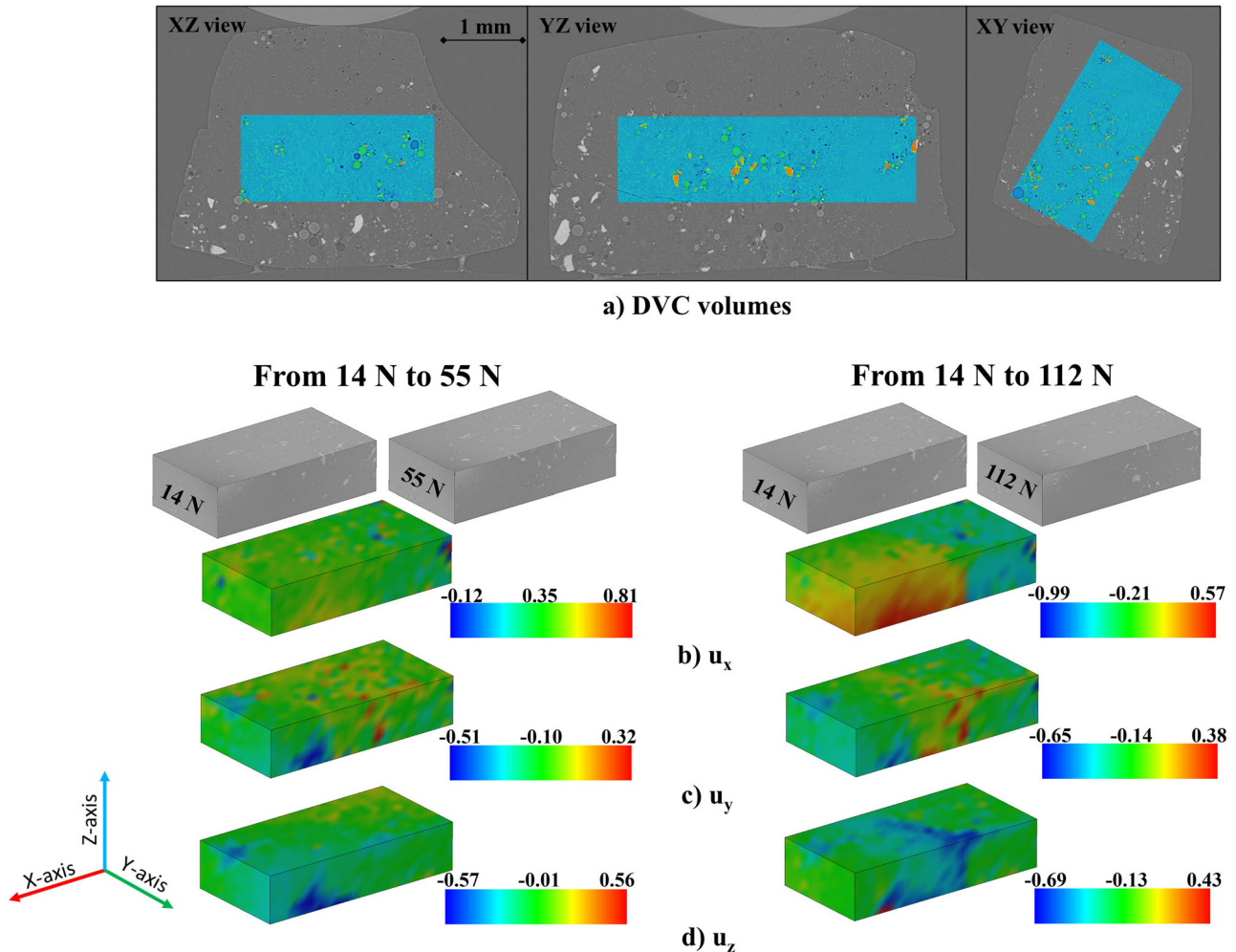


Fig. 7 Orthogonal views and images. **a** The embedded DVC volumes, corresponding DVC-measured axial displacements **b** u_x , **c** u_y and **d** u_z , developed within the MCCI-simulant volume as external loading progressively increased. Displacements are given in μm .

The resolution of the tomography scans was not optimum since the entire sample volume had to be captured within the available field-of-view. Therefore, there is a plausible scenario that the onset of microcrack formation was not captured due to the available resolution. In conjunction with the previous speculation, a compressive load-displacement curve would be key evidence to reveal material brittle or quasi-brittle behaviour. The experimental set up adopted, and the material size restrictions hindered the potential to encompass the corresponding equipment (i.e. strain gauge) and, consequently, a load-displacement curve was not feasible to be recorded.

DVC-measured data highlighted zones of localised elevated strains developed after periodically increasing the external load applied to the sample. No cracks were observed to have formed in these locations when the corresponding tomograms were inspected. In addition to qualitative conclusions, DVC-measured displacement and strain fields enabled quantification of the principal mechanical properties of the investigated sample, including the Young's modulus and Poisson's ratio. The MCCI-simulant stiffness, as expressed via the Young's modulus, is expected to lie between 15 GPa and 34 GPa, based on the methodology described in the previous sections.

It is important to mention that calculations to determine the Young's modulus range were performed assuming uniaxial compression conditions. Thus, the following equation was adopted, where E is the Young's modulus (MPa), σ_{zz}^* is the stress

equivalent of a uniaxial compression state, ΔF is the load difference (N) recorded between two loading stages, A (mm^2) is the sample surface area and ϵ_{zz} is the DVC-measured mean axial strain across the z -axis. This assumption was necessary to quantify the material Young's modulus, based on the available data [Eq. 2].

$$E = \frac{\sigma_{zz}^*}{\epsilon_{zz}} = \frac{\Delta F}{A\epsilon_{zz}} \quad (2)$$

However, Hertzian indentation differs from uniaxial compression. Considering the possible effect of such a simplification on the data, a series of FE analyses were performed to simulate the geometry of the assembly. A detailed description of this methodology, which has also been adopted to determine the Young's modulus of Chernobyl 'lava' simulants, is available in ref. ³⁴. A summary of the corresponding workflow is discussed in the following. FE analyses were performed using the software package ABAQUS. Hertzian indentation testing was performed on the MCCI-simulant. The geometry of the sample was too complex to be accurately reproduced in the FE models implemented. Therefore, a simplified cuboidal volume was generated with the DVC volume embedded. The location of the DVC volume with regards to the indenter was modelled with precision.

Realistic representation of the sample microstructure was beyond the scopes of this FE modelling work package. Therefore MCCI-simulant material was modelled as solid and homogenous. The cuboid created to simulate the entire volume was partitioned to enable visualisation of the corresponding DVC-associated

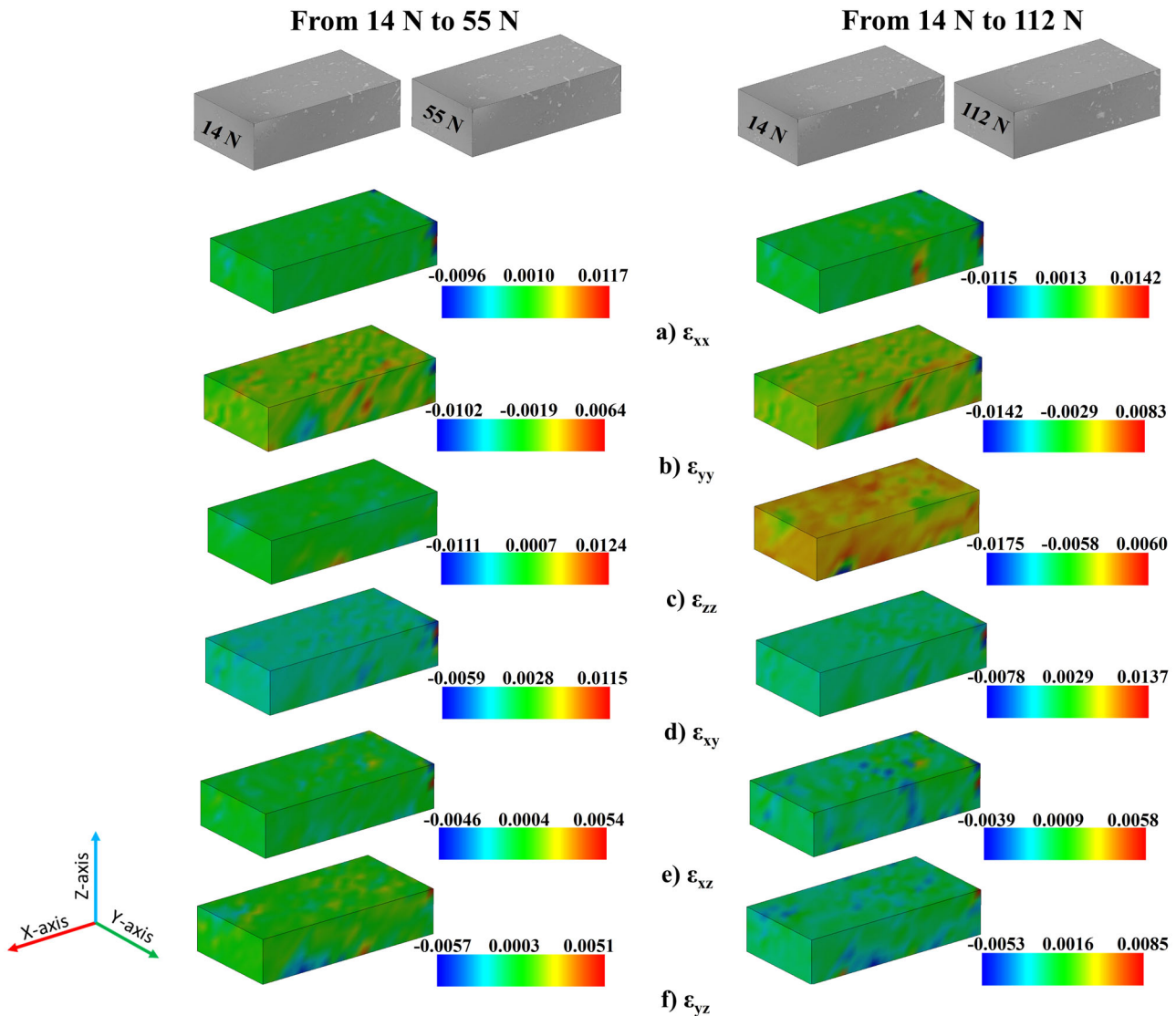


Fig. 8 DVC-measured strains developed within the MCCI-simulant volume as external loading progressively increased. **a–c** Axial DVC strains across x , y and z -axis respectively. **d–f** Shear DVC strains at XY , XZ and YZ planes, respectively.

interior volume. Three-dimensional eight-node hexagonal solid elements (C3D8) with hourglass control and reduced integration were used to build the MCCI-simulant and Hertzian indenter meshes. The indenter was modelled as a 3D discrete rigid body. Mesh sensitivity analysis was performed to determine the optimum element size. Both MCCI-simulant and ZrO_2 Hertzian indenter were modelled as isotropic, elastic materials. The Young's modulus and Poisson ratio for ZrO_2 were set equal to 210 GPa and 0.22, respectively. Since the MCCI-simulant elastic properties are unknown, a set of test values (6 GPa and 0.3 for the Young's modulus and the Poisson ratio respectively) was adopted. The base of the MCCI-simulant cuboid was fixed against all translation and rotation degrees of freedom, while body constraints were used to ensuring rigid body movement of the indenter. Surface-to-surface contact was selected to simulate the interaction properties between the indenter and the samples. Hard contact pressure-overclosure allowed surface separation under tension, and restricted node penetration under compression. A penalty contact algorithm with a friction coefficient equal to 0.5 was employed to describe the tangential behaviour of the contact properties. Prescribed vertical displacement, equal to 0.5 mm, was

implemented (displacement-controlled method) at the reference point, allowing the indenter to move only across the z -axis.

The methodology applied to determine the Young's modulus via averaging DVC-computed strains was also used to process the FE analysis results. Equation 2 was adapted and implemented to calculate the hypothetical Young's modulus value. The compressive stress $\sigma_{zz,FEM}^*$ was calculated by dividing the reaction force at a specific reference point with the upper surface of the DVC-simulated FEM cuboid, for every increment of the FE analysis. Mean vertical axial strain $\epsilon_{zz,FEM}$ was also calculated at every analysis increment, using the element strain data within the DVC-simulated cuboid mesh. A hypothetical value of Young's modulus (E_{hyp}) was derived by dividing $\sigma_{zz,FEM}^*$ with $\epsilon_{zz,FEM}$ at every increment of the analysis. No considerable variation was noted. The difference between the hypothetical Young's modulus value (E_{hyp}) and the real Young's modulus value used as input for the FE analysis (E_{FEM}), demonstrates the effect of the simplified uniaxial compression concept adopted to calculate MCCI-simulant stiffness. The ratio E_{hyp}/E_{FEM} , equal to 0.63 (± 0.0234) for this specific FEM geometry, is considered as an error control mechanism, added to the aforementioned methodology, to provide more reliable values of the MCCI-simulant Young's modulus. Thus, a

Table 1. Young's modulus calculations based on the DVC-measured data. Both displacement and strain methods were employed.

DVC run	Load transition	E, Displacement method	E, Strain method
1	14 N–55 N	18.64 GPa	15.37 GPa
2	14 N–112 N	34.54 GPa	27.60 GPa
Mean	–	26.59 (± 7.95) GPa	21.49 (± 6.11) GPa

correction factor, equal to 1.59, was applied to the Young's modulus values reported previously, to accommodate for the simplified uniaxial compression hypothesis.

The revised Young's modulus range for MCCI-simulant lies between 24 GPa and 54 GPa. This range suggests that MCCI-simulant is stiffer than the majority of brittle materials, including common ceramics (~ 3 GPa–10 GPa) and polymers (~ 1 GPa–4 GPa), and compares well with typical quasi-brittle materials such as graphite (4 GPa–28 GPa) and concrete (14 GPa–41 GPa).

To the best of our knowledge, no research performed on mechanical testing of MCCI-simulant is available. Therefore, the Young's modulus value range recommended in this paper cannot be directly compared to the relevant literature. The wide variety of phases mixed in the batch to prepare a surrogate material, combined with the unknown composition of the real material and uncertainties related to sample preparation mimicking the melt-down conditions, have proven to be a considerably complex environment for research. However, numerous studies investigating the mechanical properties of multi-phase materials relevant to MCCI have been published^{35–37}. Kitagaki et al.³⁵ investigated the fracture toughness, Young's modulus and hardness of solid mixed (U, Zr)O₂ phases. The weight percentages of UO₂ and ZrO₂ varied among the samples tested. A mean Young's modulus value equal to 182 GPa (± 26 GPa) was reported. Marchetti et al.³⁶ also synthesised mixed samples containing different percentages of UO₂ and ZrO₂ to investigate their mechanical properties using micro-echography and high-frequency acoustic microscopy. Their results were in good agreement with Kitagaki et al.³⁵, reporting a mean Young's modulus equal to 203 GPa (± 15 GPa). In addition to U-Zr containing solid samples, Marchetti et al.³⁶ performed mechanical testing on nuclear fuel debris samples bored out of the damaged Three Mile Island (TMI) Unit 2 (TMI-2) reactor core⁹. The main difference between the composition of mixed UO₂/ZrO₂ solid samples and TMI-2 nuclear fuel debris is that the latter contained a proportion of ferrous phases. The Young's modulus of TMI-2 nuclear fuel debris was found to be considerably lower (140 GPa–170 GPa) than the mixed UO₂/ZrO₂ solid samples, reflecting the effect of ferrous phases present in the material. It is believed that FDNPP MCCI contains a higher proportion of ferrous phases than does TMI-2 corium, since the steel inventories in boiling water reactors is larger than in TMI pressurised water reactors. Thus, the Young's modulus of FDNPP MCCI is expected to be considerably lower than that of TMI-2 corium, due to the higher proportion of ferrous phases present in the material.

All values reported in the literature regarding the Young's modulus of mixed U-Zr-O and fuel debris samples are significantly higher than the values presented herein for MCCI-simulant. This behaviour is attributed to the MCCI-simulant composition, which is notably different. The dominant phase present in MCCI-simulant is a SiO₂-Al₂O₃-CaO glass, where the SiO₂ fraction comprises more than 50 wt% of the sample batch composition, with an additional 24 wt% being CaO and Al₂O₃. These three phases are directly associated with the presence of a silica sand-rich cement in the FDNPP MCCI. Both mixed U-Zr-O and other fuel debris samples reported previously^{35,36} contained no phases relevant to concrete. In addition, the U-Zr-O phase comprises <14 wt% of MCCI-simulant batch mixture, while it is the dominant phase in both literature examples. We expect that the FDNPP MCCI Young's

modulus is considerably lower than that of TMI-2 corium due to the concrete presence in the solidified mixture.

A similar methodology to the one described in this paper was also adopted to determine the mechanical behaviour and microstructure of specimens manufactured to resemble the Chernobyl 'lava' materials formed within the damaged nuclear reactors after the accident there in 1986^{34,38}. The comparison between the calculated Young's moduli for the Chernobyl 'lavas' and MCCI-simulant indicates that the FDNPP material is between 1.7 \times and 2.5 \times stiffer. MCCI-simulant also exhibited a higher ($\sim 25\%$) failure load. This conclusion requires further evaluation since all specimens were of similar, but not identical, geometry.

The higher failure load, in addition to a significantly greater stiffness as noted from Young's modulus calculations, highlights the enhanced mechanical performance of MCCI-simulant, if compared to the Chernobyl 'lavas'. Given that the differences in chemical composition between the two types of simulants are not significant, this dominance can be attributed to the sample microstructure. The MCCI-simulant exhibited a significantly reduced total porosity, and pore size distribution analysis showed that, while samples contained comparable numbers of micropores (0 μm –20 μm equivalent diameter), larger pores (equivalent diameter >200 μm) were not detected in MCCI-simulant. In contrast, the 'lavas' exhibited a considerable number of larger pores, which are probably the key factor to affect the stiffness and load-bearing capacity of the material. The material segmentation analysis performed on the MCCI-simulant revealed a lower percentage of uranium-rich and iron-rich phases than in the Chernobyl 'lava' simulants. Conversely, this means that the matrix in the MCCI-simulant (rich in SiO₂), which was considerably higher in proportion than in Chernobyl 'lava' simulants, dominates the mechanical strength of the materials. It is also interesting to note that, according to Ding et al.²⁰, a range of crystalline silicate phases, including anorthite and wollastonite, as well as zircon-related cristobalite and perleveite, had formed while analysing the composition of MCCI-simulant. Such observations were not reported for the Chernobyl 'lava' simulants. It is probable that these crystalline silicate phases contribute to the enhanced mechanical properties noted for MCCI-simulant, if compared with Chernobyl 'lavas'. Corroborating the previous hypothesis, wollastonite presence in concrete mixes has proven to increase the material strength³⁹.

The restriction to access real Fukushima MCCI samples could raise concerns about the compatibility between real samples formed after the accident and lab-fused surrogates. Chernobyl 'lava' simulant samples fabricated under a similar methodology¹⁵ exhibited comparable microstructure with real 'lava' samples⁴, enhancing the validity of the process followed to investigate MCCI-simulant samples. The effect of irradiation on the material mechanical behaviour needs to be considered. Studies performed on irradiated concrete samples demonstrated a reduction in both compressive and tensile strength when compared to virgin concrete⁴⁰. Since the presence of crystalline phases associated with cement is dominant within the material volume, MCCI mechanical strength is expected to decline throughout the years, due to irradiation. Replacement of Pu with Ce in the MCCI-simulant can affect material properties, since it is possible that mechanisms of Pu-(U)-O-Si phase formation differ to corresponding Ce-(U)-O-Si. However, reaction between PuO₂ and SiO₂ has

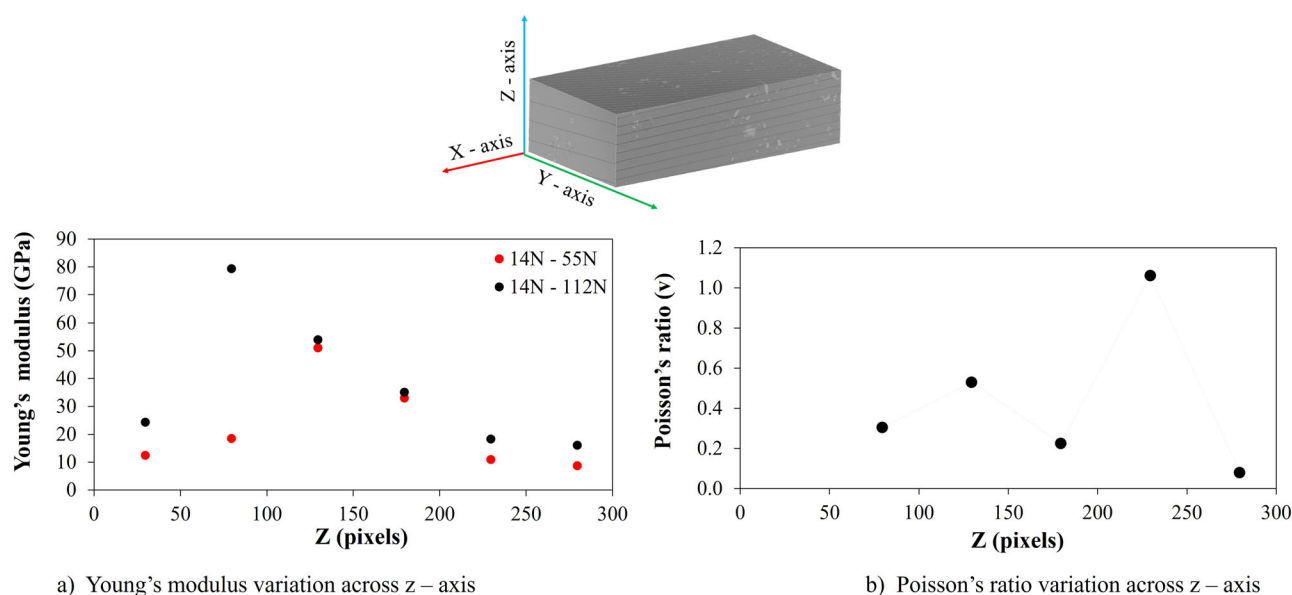


Fig. 9 Variation in MCCI-simulant mechanical properties across the height of the DVC-inspected volume based on calculated mean XY planar vertical strains. **a** Young's modulus. **b** Poisson's ratio.

been reported in corresponding studies, leading to formation of Pu-percleveite, in compliance with Ce-percleveite formed during the fabrication of MCCI-simulant used in these studies.

The effect of MCCI long-term interaction with water on the material mechanical properties needs to be considered. Relevant work performed on Chernobyl "lavas"⁴⁻⁶, revealed considerable chemical alteration to have occurred after interaction with water. "Lavass" composition is expected to be relevant to Fukushima MCCI, even if the accident conditions and materials involved slightly differ. The abundance of ferrous inclusions within the MCCI volume, associated with 316 stainless steel piping, is a key issue to consider. It is likely that these metallic inclusions are corroded throughout this decade, not only during initial short-term interaction with seawater but also during subsequent interaction with cooling water. Corrosion of Fe-bearing phases is always accommodated with volume expansion, regardless of the identity of the corrosion products. Volume expansion coefficient may vary between 1.70 up to 6.15⁴¹. Corrosion-induced volume expansion of ferrous phases within the MCCI volume is a potential that raises concerns about the material mechanical behaviour. Potential cracks formation, induced by this internal volume expansion, can drastically affect the integrity and, consequently, the mechanical strength. In addition, mechanically unstable ZrO₂, which is highly probable to be present within the MCCI volume, could also act as a source for crack generation since potential transformation from tetragonal to monoclinic phase is associated with volume expansion⁶. The effect of cracks presence in the embedded MCCI on the material stiffness and strength, need to be highly evaluated prior to decommissioning. Therefore, the scenario of a revised and reduced Young's modulus value, reflecting the event of a cracked material core should be considered.

The DVC-measured strain fields were also used to estimate the range of Poisson's ratio for MCCI-simulant. Calculations were performed considering, at first, entire probed volume and secondly divided volumes. The latter enabled investigation of the Poisson's ratio distribution across the sample height. A significant scatter of values was observed even among those lying within the range of a continuum (0–0.5). It is believed that this behaviour is attributed to the heterogenous sample micro-structure. Parts of the divided volumes used for the analysis were

considerably less porous than others, reflecting the strong diversity noticed in the corresponding mean strain values.

To summarise, the main findings of the research performed and presented in this paper are outlined below:

- Based on the observations made throughout mechanical testing and the quantitative analysis performed using the XCT data, there is no adequate findings to classify the material as either brittle or quasi-brittle. Additional work is required to extract more valid conclusions.
- DVC-processed data revealed locations of elevated axial and shear strains, indicating potential failure zones for the material with no signs of damage being detected in the corresponding tomograms.
- The Young's modulus of MCCI-simulant is expected to lie between 24 GPa and 54 GPa. Poisson's ratio calculations exhibited a significant scatter, even within the range for a continuum.
- MCCI-simulant exhibits a lower total porosity and higher stiffness compared to Chernobyl 'lavass'.
- Effect of MCCI long-term interaction with water on the material mechanical behaviour should be taken into consideration.

METHODS

Materials and sample preparation

Full details of the simulant MCCI synthesis and characterisation are given in Ding et al.²⁰. The batched compositions were based on estimations of the relative proportions of core materials and concrete, previously reported in the literature and through discussion with personnel at the Japan Atomic Energy Agency^{42,43}. The as-batched reagent stoichiometry included SiO₂, CaO and Al₂O₃ as components of the sand-rich cement mortar utilised in the reactor construction, Fe₂O₃ and 316 stainless steel (Fe/Cr₁₈/Ni₁₀/Mo₃) to represent the steel components of the reactor units and (U,Zr,Ce)O₂ as an oxidised fuel/cladding surrogate (with Ce acting as a surrogate for Pu from mixed-oxide fuel within Unit 3). Zr was also added separately as ZrO₂. The mixed batch was sintered under a reducing atmosphere (5% H₂/95% N₂) at 1500 °C for 4 h, and then 720 °C for 72 h to promote crystalline grain growth. A heating and cooling rate of 3 °C min⁻¹ was utilised.

Mechanical loading

The radioactive nature of MCCI-simulant restricted the range of suitable mechanical loading methods. In compliance with relevant studies on brittle and quasi-brittle materials^{27,44}, Hertzian indentation was found to be the most appropriate method since only mm-scale specimens could be used for testing. A bespoke mechanical rig was assembled to comply with the experimental requirements and the sample dimensions. The Hertzian indenter was composed of a single 5 mm diameter ZrO₂ sphere adhered to a cylindrical steel holder. Manual rotation of a metallic rod, attached to the rig's top flange and connected with the indenter, favoured movement of the entire assembly across the vertical axis. The sample holder was placed in line with the indenter assembly, ensuring that loading was imposed on the centre of the sample top surface. A miniature USB button-type load-cell was located beneath and in line with the sample holder and the indenter assembly to measure the compressive reaction force as external load was applied. The rig was manufactured to be used on the I12 beamline, a research facility at DLS⁴⁵ suitable for synchrotron X-ray imaging and diffraction analysis. Polycarbonate was selected to construct the rig's containment walls and the sample holder, thanks to its low X-ray attenuation, high flex modulus and tensile strength⁴⁶. One single MCCI-simulant sample (107.7 mg) of roughly cuboidal shape was mechanically tested. Sample geometry imperfections were inevitable due to the preparation method followed and the machining process. Experiment feasibility requirements, as well as radioactivity limits and allocated beamtime restrictions, enforced minimisation of the number and size of the samples to be used in situ.

Synchrotron X-ray tomography

Changes in sample microstructure due to progressively increased external loading were monitored using synchrotron XCT on I12 beamline at the DLS⁴⁵. The combination of high flux and energies available in this specific beamline matched the requirements for optimum quality imaging. XCT scans were performed at all stages of the stepwise Hertzian indentation process. The monochromatic X-ray beam was tuned to 101.97 keV. Probing the entire sample volume was essential to reveal the magnitude of mechanical degradation. Therefore, camera optics with a field-of-view of 8.0 mm × 7.0 mm were selected. The corresponding pixel size was 3.25 μm, enabling tracing of microstructural features. Exposure time was set equal to 0.4 s, with a total of 3000 projections acquired per scan. Data reconstruction was conducted using the open-source software Savu⁴⁷. Avizo³¹, a commercial software application for data visualisation and analysis, was also employed for advanced data processing, 3D volume rendering and phase volume segmentation.

Experimental process

Ex situ trials were performed to optimise the experimental procedure and set up the plan for in situ mechanical testing. The loading sequence pursued on the I12 beamline was determined based on these ex situ tests. The typical experimental route adopted included stepwise loading followed by successive XCT scans at each loading stage. This process was repeated until the sample failed. Sudden drops of force output during manual load topping-up were treated as indicators of sample failure. All XCT scans were acquired without moving the ZrO₂ indenter away from the sample. This was validated by the force output recorded by the load-cell, which remained constant throughout the scanning process. The only exceptions were a couple of control scans, one performed before imposing any external loading on the sample and the other at the end of experimentation. This pair of scans was acquired with the indenter retracted. Force relaxation occurred immediately after the peak load was established. However, only insignificant load fluctuation was recorded during XCT scan acquisition.

DATA AVAILABILITY

The raw/processed data required to reproduce these findings cannot be shared at this time as the data also form part of an ongoing study.

Received: 21 December 2021; Accepted: 8 June 2022;

Published online: 07 July 2022

REFERENCES

- Nuclear damage compensation and decommissioning facilitation corporation. Technical strategic plan 2016 for decommissioning of the Fukushima Daiichi nuclear power station of Tokyo Electric Power Company Holdings, 2016. https://www.dd.nfd.go.jp/files/topics/449_ext_02_0.pdf - [Accessed 21/04/2022].
- Grambow, B. & Mostafavi, M. State of Fukushima nuclear fuel debris tracked by Cs137 in cooling water. *Environ. Sci. Process* **16**, 2472–2476 (2014).
- Summary of decommissioning and contaminated water management. TEPCO, 2018. https://www.tepco.co.jp/en/nu/fukushima-np/roadmap/images/d180201_01-e.pdf [Accessed 21/04/2022].
- Zubekhina, B. et al. Long-term aging of Chernobyl fuel debris: Corium and “Lava”. *Sustainability* **13**, 1073 (2021).
- Zubekhina, B. Y. & Burakov, B. E. Leaching of actinides and other radionuclides from matrices of Chernobyl “lava” as analogues of vitrified HLW. *J. Chem. Thermodyn.* **114**, 25–29 (2017).
- Shiryaev, A. A. et al. Study of mineral grains extracted from the Chernobyl “lava”. *Miner. Pet.* **114**, 489–499 (2020).
- Reactor imaging technology for fuel debris detection by cosmic ray muon Measurement status report in Unit-1. TEPCO, 2015. http://www.tepco.co.jp/en/nu/fukushima-np/handouts/2015/images/handouts_150319_01-e.pdf - [Accessed 21/04/2022].
- Ochiai, A. et al. Uranium dioxides and debris fragments released to the environment with Cesium-rich microparticles from the Fukushima Daiichi nuclear power plant. *Environ. Sci. Technol.* **52**, 2586–2594 (2018).
- Bottomley, P. D. & Coquerelle, M. Metallurgical examination of bore samples from the Three Mile Island Unit 2 reactor Core. *Nucl. Technol.* **87**, 120–136 (1989).
- Olsen, C. S., Jensen, S. M., Carlson, E. R. & Cook, B. A. Materials Interactions and temperatures in the Three Mile Island Unit 2 Core. *Nucl. Technol.* **87**, 57–94 (1989).
- Shiryaev, A. A. et al. Physico-chemical properties of Chernobyl lava and their destruction products. *Prog. Nucl. Energy* **92**, 104–118 (2016).
- Burakov, B. E., Strykanova, E. E. & Anderson, E. B. Secondary uranium minerals on the surface of Chernobyl “Lava”. *MRS Proc.* **465**, 1309 (1997).
- Grambow, B. & Poinssot, C. Interactions between nuclear fuel and water at the Fukushima Daiichi reactors. *Elements* **8**, 213–219 (2012).
- Takano, M. & Nishi, T. High temperature reaction between sea salt deposit and (U,Zr)O₂ simulated corium debris. *J. Nucl. Mater.* **443**, 32–39 (2013).
- Barlow, A. et al. Synthesis of simulant “lava-like” fuel containing materials (LFCM) from the Chernobyl reactor Unit 4 meltdown. *MRS Adv.* **2**, 1–6 (2017).
- Song, J., Min, B., Hong, S., An, S. & Hong, S. An investigation on the physical and chemical behaviors of fuel debris during severe accident progression. *Prog. Nucl. Energy* **106**, 345–356 (2018).
- An, S. M., Song, J. H., Kim, J. Y., Kim, H. & Naitoh, M. Experimental investigation on molten pool representing corium composition at Fukushima Daiichi nuclear power plant. *J. Nucl. Mater.* **478**, 164–171 (2016).
- Pellegrini M, et al. Benchmark study of the accident at the Fukushima Daiichi NPS best estimate case comparison. Nureth-16, Chicago, IL, 2015. <http://glc.ans.org/nureth-16/data/papers/13743.pdf> - [Accessed 21/04/2022].
- Nagase, F., Gauntt, R. O. & Naito, M. Overview and outcomes of the OECD/NEA benchmark study of the accident at the Fukushima Daiichi nuclear power station. *Nucl. Technol.* **196**, 499–510 (2016).
- Ding, H. et al. Chemical characterisation of degraded nuclear fuel analogues simulating the Fukushima Daiichi nuclear accident. *Npj. Mater. Degrad.* **6**, 10 (2022).
- Bay, B. K., Smith, T. S., Fyhrie, D. P. & Saad, M. Digital volume correlation: three-dimensional strain mapping using x-ray tomography. *Exp. Mech.* **39**, 217–226 (1999).
- Bay, B. K. Methods and applications of digital volume correlation. *J. Strain Anal. Eng. Des.* **43**, 745–760 (2008).
- Buljac, A. et al. Digital volume correlation: Review of progress and challenges. *Exp. Mech.* **58**, 661–708 (2018).
- Wang, B., Sun, L. & Pan, B. Mapping internal deformation fields in 3D printed porous structure with digital volume correlation. *Polym. Test.* **78**, 105945 (2019).
- Forna-Kreutzer, J. P. et al. Full-field characterisation of oxide-oxide ceramic-matrix composites using X-ray computed micro-tomography and digital volume correlation under load at high temperatures. *Mater. Des.* **208**, 109899 (2021).
- Mostafavi, M. et al. Yield behavior beneath hardness indentations in ductile metals, measured by three-dimensional computed X-ray tomography and digital volume correlation. *Acta Mater.* **82**, 468–482 (2015).
- Vertyagina, Y., Mostafavi, M., Reinhard, C., Atwood, R. & Marrow, T. J. In situ quantitative three-dimensional characterisation of sub-indentation cracking in polycrystalline alumina. *J. Eur. Ceram. Soc.* **34**, 3127–3132 (2014).
- Mostafavi, M. et al. Three-dimensional crack observation, quantification and simulation in a quasi-brittle material. *Acta Mater.* **61**, 6276–6289 (2013).

29. Yang, Z. et al. In-situ X-ray computed tomography characterisation of 3D fracture evolution and image-based numerical homogenisation of concrete. *Cem. Concr. Compos.* **75**, 74–83 (2017).
30. Mostafavi, M., McDonald, S. A., Mummery, P. M. & Marrow, T. J. Observation and quantification of three-dimensional crack propagation in poly-granular graphite. *Eng. Fract. Mech.* **110**, 410–420 (2013).
31. AVIZO, AVIZO User's Guide, 2018.
32. Barhli, S. M. et al. Synchrotron X-ray characterization of crack strain fields in polygranular graphite. *Carbon* **124**, 357–371 (2017).
33. Ferreira T, Rasband W. ImageJ user guide 1.46r. 2012.
34. Paraskevoulakos, C. et al. Investigating the microstructure and mechanical behaviour of simulatant “lava-like” fuel containing materials from the Chernobyl reactor unit 4 meltdown. *Mater. Des.* **201**, 109502 (2021).
35. Kitagaki, T. et al. Mechanical properties of cubic (U,Zr)O₂. *J. Nucl. Eng. Radiat. Sci.* **4**, 031011 (2018).
36. Marchetti, M. et al. Elastic properties of severely degraded fuels. *J. Nucl. Mater.* **529**, 151918 (2020).
37. Veit, U. & Rüssel, C. Density and Young's Modulus of ternary glasses close to the eutectic composition in the CaO-Al₂O₃-SiO₂-system. *Ceram. Int.* **42**, 5810–5822 (2016).
38. Barlow, S. T. et al. Synthesis, characterisation and corrosion behaviour of simulatant Chernobyl nuclear meltdown materials. *Npj. Mater. Degrad.* **4**, 1–8 (2020).
39. Mathur, R., Misra, A. K. & Goel, P. Influence of wollastonite on mechanical properties of concrete. *J. Sci. Ind. Res.* **66**, 1029–1034 (2007).
40. Vodák, F., Trtik, K., Sopko, V., Kapičková, O. & Demo, P. Effect of γ -irradiation on strength of concrete for nuclear-safety structures. *Cem. Concr. Res.* **35**, 1447–1451 (2005).
41. Jamali, A., Angst, U., Adey, B. & Elsener, B. Modeling of corrosion-induced concrete cover cracking: a critical analysis. *Constr. Build. Mater.* **42**, 225–237 (2013).
42. Kitagaki, T., Yano, K., Ogino, H. & Washiya, T. Thermodynamic evaluation of the solidification phase of molten core–concrete under estimated Fukushima Daiichi nuclear power plant accident conditions. *J. Nucl. Mater.* **486**, 206–215 (2017).
43. Tanabe, F. Analysis of core melt accident in Fukushima Daiichi-Unit 1 nuclear reactor. *J. Nucl. Sci. Technol.* **48**, 1135–1139 (2011).
44. Saucedo-Mora, L. et al. Observation and simulation of indentation damage in a SiC-SiC fibre ceramic matrix composite. *Finite Elem. Anal. Des.* **110**, 11–19 (2016).
45. Drakopoulos, M. et al. I12: the Joint Engineering, Environment and Processing (JEEP) beamline at Diamond Light Source. *J. Synchrotron Radiat.* **22**, 828–838 (2015).
46. Michaelsen, K. et al. Characterization of materials for optimal near-infrared and x-ray imaging of the breast. *Biomed. Opt. Express* **3**, 2078 (2012).
47. Atwood, R. C., Bodey, A. J., Price, S. W. T., Basham, M. & Drakopoulos, M. A high-throughput system for high-quality tomographic reconstruction of large datasets at Diamond Light Source. *Philos. Trans. R. Soc. A. Math. Phys. Eng. Sci.* **373**, 20140398 (2015).

ACKNOWLEDGEMENTS

The presented work is part of the CHIMP programme, funded by EPSRC. This research was a joint UK-Japan effort to support ongoing clean-up operations at the Fukushima

Daiichi Nuclear Power Plant (funder reference: EP/R01924X/1). The authors would like to thank Diamond Light Source Ltd for awarding beamtime (EE20189-1) and the entire team of the DLS I12 beamline for supporting this research. M.M. acknowledges the support of the Royal Academy of Engineering through a Senior Research Fellowship and EPSRC (grant number EP/R013047/1). C.L.C. wishes to acknowledge EPSRC for funding through an Early Career Research Fellowship (grant number EP/N017374/1). J.P.F.-K. and D.L. would like to acknowledge the EPSRC Grants EP/L016028/1 and EP/T000368/1, respectively.

AUTHOR CONTRIBUTIONS

C.P.: Conceptualisation, Methodology, Software, Formal Analysis, Investigation, Writing—Original Draft, Writing—Review & Editing. J.F.-K.: Methodology, Software. K.R.H.: Investigation, Writing—Review & Editing. C.P.J.: Investigation. T.B.S.: Writing—Review & Editing. C.G.: Investigation. D.L.: Software, Writing—Review & Editing. C.R.: Investigation. C.L.C.: Conceptualisation, Funding Administration. M.M.: Conceptualisation, Funding Administration.

COMPETING INTERESTS

The authors declare no competing interests.

ADDITIONAL INFORMATION

Correspondence and requests for materials should be addressed to Charilaos Paraskevoulakos.

Reprints and permission information is available at <http://www.nature.com/reprints>

Publisher's note Springer Nature remains neutral with regard to jurisdictional claims in published maps and institutional affiliations.



Open Access This article is licensed under a Creative Commons Attribution 4.0 International License, which permits use, sharing, adaptation, distribution and reproduction in any medium or format, as long as you give appropriate credit to the original author(s) and the source, provide a link to the Creative Commons license, and indicate if changes were made. The images or other third party material in this article are included in the article's Creative Commons license, unless indicated otherwise in a credit line to the material. If material is not included in the article's Creative Commons license and your intended use is not permitted by statutory regulation or exceeds the permitted use, you will need to obtain permission directly from the copyright holder. To view a copy of this license, visit <http://creativecommons.org/licenses/by/4.0/>.

© The Author(s) 2022